RSC Advances

ROYAL SOCIETY OF CHEMISTRY

www.rsc.org/advances

Revealing the Unfavorable Role of Superfluous $CH_3NH_3PbI_3$ Grain Boundary Traps in Perovskite Solar Cells on Carriers Collection

Yangyang Du, Hongkun Cai, * Hongbin Wen, Yuxiang Wu, Zhenglong Li, Jian Xu, Like Huang, Jian Ni, Juan Li, Jianjun Zhang

College of Electronic Information and Optical Engineering, Nankai University, Key Laboratory of Opto-electronic Information Science and Technology for Ministry of Education, Tianjin, 300071, China

ABSTRACT: In this work, a facile sequential thermal evaporation strategy in low vacuum (STELV) is proposed to fabricate good crystallization $CH_3NH_3PbI_3$ films with controllable grain size. Through a comparative study, it is observed that the photovoltaic parameters of perovskite solar cells (PSCs) are closely related to $CH_3NH_3PbI_3$ grain size and large grains should contribute to superior performance and small hysteresis index. Also, we demonstrate that the declining performance should be ascribed to high carrier combination rate caused by superfluous perovskite grain boundary (PGB) traps. By the combination with Silvaco simulation software based on physical models, the recombination rate distribution within PSCs is clearly observed. In addition, lateral conduction band energy distribution within $CH_3NH_3PbI_3$ films and the transient carrier collection efficiency are also performed suggesting that PGB traps are prominently responsible for inferior device performance by leading to serious lateral transport of photo-generated carriers and reducing their collection efficiency, which are consistent with experimental result.

KEYWORDS: Perovskite solar cells (PSCs), STELV, perovskite grain boundary (PGB), recombination, $CH_3NH_3PbI_3$, hysteresis.

1. INTRODUCTION

Organic-inorganic halide perovskites (e.g. $CH_3NH_3PbI_3$ or $CH_3NH_3PbI_{3-x}Cl_x$) have increasingly excited research community around the world as one of the most appealing materials for

photovoltaic application during the past few years owing to their fascinating characteristics such as high absorption coefficient (>10^4 cm^{-1}), [1] long carrier diffusion length (100-1000 nm), [2] tunable optical band gaps [3-6] as well as simple and low-cost spin coating technology. [5-10] To date, the development of PSCs have witnessed tremendous progress. The certified champion efficiency for PSCs by NREL has reached 22.1%, rivaling that of single crystal silicon solar cells. In addition, snaith *et al.* have recently presented highly crystalline and photostable perovskite material by replacing organic $CH_3NH_3^+$ ion with hybrid organic $HC(NH_2)_2^+$ and inorganic Cs^+ ions, which is further combined with silicon cell achieving >25% four terminal tandem cells. [4] Meanwhile, a few groups have constantly revealed the origin of poor stability for perovskite films, including temperature, [11,12] ambient humidity, [13] and light and oxygen induction. [14] As such, long-term stability tests for PSCs stored in air at room temperature without encapsulation are carried out for over 1000 hrs under full sun light, [8,12,15,16] which shows their promising future practical application.

Presently, although a plethora of innovative approaches on fabricating $CH_3NH_3PbI_3$ films have been proposed in most literature reports including one-step deposition, [5-8] sequential deposition [16-18] and evaporation deposition in high vacuum, [19] one of the most crucial issues for PSCs to be addressed is the morphology and grain size control of $CH_3NH_3PbI_3$ layer playing a crucial role in PSCs performance. [6,20] Moreover, Huang et al. and Ohkita el al. have revealed that numerous perovskite grain boundary (PGB) should have a unfavorable role on PSCs performance due to possessing superfluous charge traps. [21-22] Unfortunately, it is well recognized that $CH_3NH_3PbI_3$ films fabricated by aforementioned methods often exhibit wide variations in $CH_3NH_3PbI_3$ grain size. [20] Worse still, $CH_3NH_3PbI_3$ films also exhibit extensive fluctuation in grain size even

prepared by identical process conditions. To reduce the number of PGB trap density caused by various grain size, some efforts consequently have been attempted by passivating or enlarging grain size. [23-24] In particular, increasing $CH_3NH_3PbI_3$ grain is appealing [20,24,25] and the monomeric size of PSCs has broken through 1 cm^2 as well. [8] On the other hand, the majority of reported approaches for preparing $CH_3NH_3PbI_3$ films are either restricted in glove boxes filled with nitrogen or high vacuum atmosphere that they naturally increase fabrication cost of PSCs. It is therefore necessary that an approach for preparing controllable $CH_3NH_3PbI_3$ grain via low cost should be proposed.

Additionally, despite of the fact that PGB traps should be responsible for many unusual electrical behaviors within PSCs demonstrated by experimental progress, [20,21,25,26,27] understanding the origin of their role however is very limited. Also, some fundamental physical mechanism about PSCs is still confusing and the related theory mentioned in some reported literature is also lack of evidence.

Herein, we firstly report a facile sequential thermal evaporation strategy in low vacuum (STELV) for fabricating $CH_3NH_3PbI_3$ films with controllable grain size, in which PbI_2 and CH_3NH_3I powder are subsequently deposited on compact TiO_2 substrate in low vacuum, followed by solid-state rapid insertion reaction during the process of annealing at 150 ℃ in virtue of high concentration gradient of CH_3NH_3I. Incorporation them into PSCs, the photovoltaic parameters having distinct difference are attained with the variation of $CH_3NH_3PbI_3$ grain size. To get a better view of these difference, fundamental recombination behavior within PSCs are carefully investigated with the help of Silvaco simulator software. Furthermore, the lateral conduction band energy distribution, and transient carrier collection efficiency are also exhibited, which cannot be

easily achieved by routine measurements, demonstrating that superfluous carrier transport across lateral direction occurs when PGB trap density is high (>1e14 cm^{-3}) and large $CH_3NH_3PbI_3$ grains are necessary for efficient PSCs.

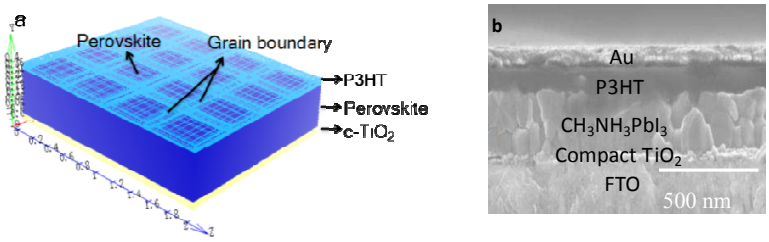

Fig.1 (a) Overall meshed PSCs simulation structure illustration including PGB region; (b) The cross-section scanning electron microscope (SEM) image corresponding to planar PSCs construction including FTO/compact TiO_2/$CH_3NH_3PbI_3$/P3HT/Au.

2. EXPERIMENTAL METHODS

Characterization. The surface and cross section morphology of $CH_3NH_3PbI_3$ films were observed by scanning electron microscope (SEM) (Hitachi SU8010). The X-ray diffraction（XRD）（Philips PANalytical X’Pert Pro, Cu Kα）was used to acquire the $CH_3NH_3PbI_3$ crystal orientation. The $CH_3NH_3PbI_3$ absorption spectra were measured by a UV-VIS spectrophotometer (Cary 5000). The PL spectrum of $CH_3NH_3PbI_3$ films were recorded using a steady-state fluorescence spectrometer (FL3-2-IHR221-NIR-TCSPC). The current density-voltage (J-V) characteristics of PSCs were measured with a Abet sun 2000 solar simulator under the illumination of an AM 1.5G (100 mW/cm^2) at regular time intervals (0.02 V/S scan speed). The electrochemical impedance spectroscopy (EIS) (METEK) was employed to characterize the transfer dynamics of PSCs. The external quantum efficiency (EQE) spectrum was tested to demonstrate the photoelectricity response of PSCs.

Device fabrication. The PSCs were prepared according to the construction shown in Fig. 1a and b. Firstly, the neat FTO glasses substrate were washed with mixed solution of ethanol and

acetone (1：1 volume ratio) via sonication for 15 min, and then sequentially washed with isopropanol for 15 min. Prior to depositing compact TiO_2 film, FTO substrates were treated in a UV-ozone clearer for 12 min. About 50 nm thick compact TiO_2 was formed on the cleaned FTO glass by sol-gel method according to our previous report. [7] With regard to the $CH_3NH_3PbI_3$ film fabricated by STELV, 50 mg PbI_2 power was firstly evaporated on substrate via thermal evaporation in low vacuum (~ 1 Pa) with 60 A evaporation current, and subsequently superfluous CH_3NH_3I powder was evaporated on the formed PbI_2 film to make sure the fully transformation form PbI_2 to $CH_3NH_3PbI_3$. The adoption of 50 mg PbI_2 was available to attain a optimized $CH_3NH_3PbI_3$ thickness. During the process of annealing at 150 ℃, $CH_3NH_3PbI_3$ film was assembled with the interaction and interdiffusion between solid-state PbI_2 and CH_3NH_3I components. Finally, the formed $CH_3NH_3PbI_3$ film was washed with isopropanol to remove redundant CH_3NH_3I. A higher annealing temperature compared with common reports was adopted because a higher temperature could be beneficial role on forming large $CH_3NH_3PbI_3$ grains. [20,24] And higher temperature should facilitate the interdiffusion reaction and crystallization. In order to control the $CH_3NH_3PbI_3$ grain size by STELV, the evaporation rate was controlled by changing evaporation current. Furthermore, a P3HT solution was prepared by dissolving 15 mg P3HT in 1 ml chlorobenzene, to which 18 ul of lithium bis (trifluoromethanesulfony) imide (LiTFSI) solution (280 mg/ml acetonitrile) and 10 ul of 4-tert-butylpyridine were added. The hole-transport layer was prepared by spin-coating P3HT solution at 3000 rpm for 40s. Finally, a 150 nm thick gold counter electrode was deposited by thermal evaporation and the dot area of PSCs was 0.06 cm^2.

3. RESULTS AND DISCUSSION

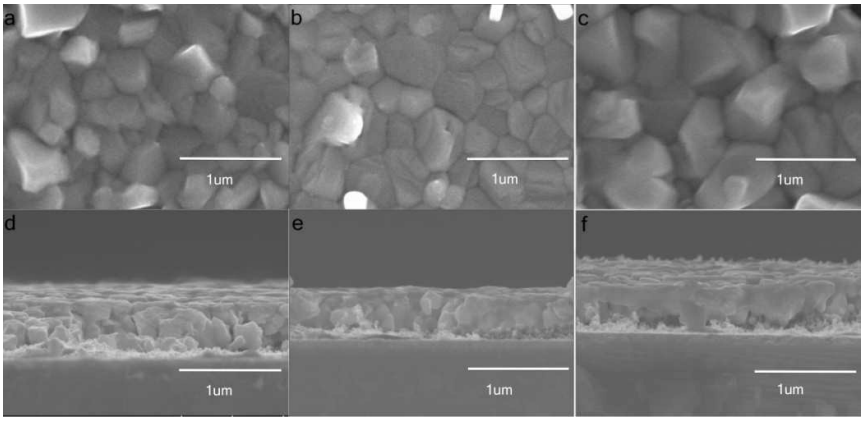

Fig. 2 The SEM and cross-section SEM images of $CH_3NH_3PbI_3$ films prepared by STELV procedure with different value of evaporation current. (a,d) 70 A; (b,e) 65 A; (c,f) 60 A, respectively.

The evaporation rate strongly affected the growth rate of $CH_3NH_3PbI_3$ film, and thereby varying $CH_3NH_3PbI_3$ grain size. Initially, SEM was conducted to observe the $CH_3NH_3PbI_3$ grain size prepared by STELV and Fig. 2 showed the surface and corresponding cross section morphology of $CH_3NH_3PbI_3$ films prepared at 70 A, 65 A, and 60 A evaporation current, respectively. It was absolutely noted that under the same length scale, there were smaller grains in the sample prepared at 70 A, showing that a higher evaporation current went against producing large $CH_3NH_3PbI_3$ grains. Besides, the average $CH_3NH_3PbI_3$ grain size greatly increased with decreasing the evaporation current owing to a low evaporation rate, which might be related to the volume expansion as demonstrated by Zhao et al.. [17] As shown in Fig. 2, it could be estimated that grain size were about 250 nm, 350 nm and 600nm, corresponding to 70 A, 65A and 60 A evaporation current respectively. Apart from the variation of grain size, all samples exhibited dense morphology facilitating the reduction of leakage current. [7] In order to obtain a more precise validation of perovskite structure, the corresponding XRD evolution pattern were displayed in Fig. S1, in which two preferential XRD diffraction peaks at 14.17° and 28.51° were detected, assigned to (110) and (220) tetragonal perovskite crystal planes. The full width at half maximum of (110)

diffraction peak was reduced as the evaporation current decreased from 70 A to 60 A, which were in good agreement with the result observed in SEM. In addition, the UV-vis absorption spectra of the $CH_3NH_3PbI_3$ samples were also shown in Fig. S2, in which all films exhibited nearly identical absorption situation owing to the same thickness value determined by the cross section SEM measurement shown in Fig. S3.

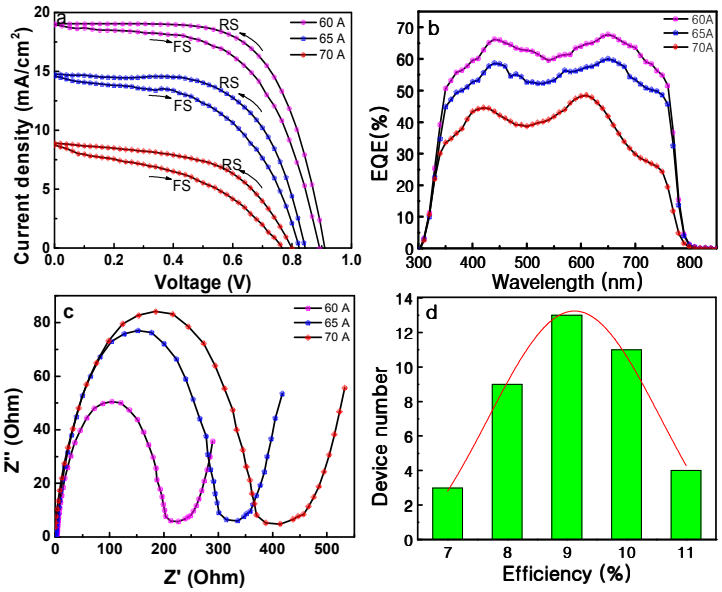

Fig. 3 Efficiency measurements. (a) J-V curves for PSCs without encapsulation with FS and RS direction in light respective; (b) EQE spectrum for corresponding devices; (c) Nyquist plots at V=1.0 v for corresponding devices; (d) Histogram of efficiency distribution for 40 devices based on 60 A evaporation current.

Table 1. Photovoltaic parameters derived from J-V measurements corresponding to Fig. 3a

sample	J_{sc}(mA/cm^2)	V_{oc}(V)	FF (%)	PCE (%)	HI
60 A	19.09	0.91	64.7	11.24	0.133
65 A	14.72	0.84	62.1	7.68	0.188
70 A	8.87	0.80	54.3	3.85	0.299

Then, to examine the impact of $CH_3NH_3PbI_3$ grain size on device performance, the prepared $CH_3NH_3PbI_3$ films were used to assemble planar PSCs with a configuration shown in Fig. 1b. Fig. 3a showed J-V curves of PSCs obtained from short-circuit to open-circuit scanning direction (FS), and from open-circuit to short-circuit scanning direction (RS). All the measurements for J-V

curves were carried out at regular time intervals (0.02 V/s scan rate) in air atmosphere and the corresponding parameters were concluded in Table 1 that included the parameter of hysteresis index (HI) defined by equation 1 to numerically confirm the degree of hysteresis. $J_{RS}(0.8V_{oc})$ and $J_{FS}(0.8V_{oc})$ represent the value of current density at $0.8V_{oc}$ with RS and FS direction respectively. As shown in Fig. 3a, it did exhibit authentic J-V hysteresis situation that the determined efficiency was so strongly dependent on voltage scanning direction, which generally was interpreted to be due to the influence of defects, charge selective contacts, ions mobility, ferroelectricity.[26-28] The device possessing small grain size showed larger hysteresis index compared with the large ones (under identical other conditions), which indicated that the smaller perovskite grain size the severer J-V hysteresis. In order to further understand the relationship between hysteresis and perovskite grain size, more discussion were conducted in the back section. On the other hand, the overall device performance obviously declined when the perovskite grain size decreased form 600 nm to 250 nm devoid of scanning direction. Meanwhile, the corresponding EQE was shown in Fig. 3b, which also exhibited the same descending trend with decreasing grain size. Considering the parallel absorption spectrum (shown in Fig. S2), it was therefore justified that the inferior current should be ascribed to poor carrier collection, coming from high recombination resulting from rich PGB trap density. Furthermore, electrochemical impedance spectroscopy (EIS) was employed to characterize PSCs charge transfer dynamics and corresponding nyquist plots were shown in Fig. 3c. The first semicircle pointed out the strong interfacial influence consisting of compact $TiO_2/CH_3NH_3PbI_3$/P3HT.[29,30] Hence, the increased resistance at the first semicircle ranging from 225 ohm to 414 ohm would illustrate increasing transport resistance at whole device, which validated the decrease of fill factor (FF). As a consequence, it was unveiled that overall device

performance were declining as $CH_3NH_3PbI_3$ grain size decreased. Finally, we counted PSCs performance distribution based on 60A evaporation current for 40 devices, whose average and standard deviation for 40 devices were 0.85% and 1.1% respectively, estimated from histogram of efficiency distribution (shown in Fig. 3d) indicating favorable PSCs reproducibility fabricated by STEVL.

$$HI = \frac{J_{RS}(0.8V_{oc}) - J_{FS}(0.8V_{oc})}{J_{RS}(0.8V_{oc})} \quad (1)$$

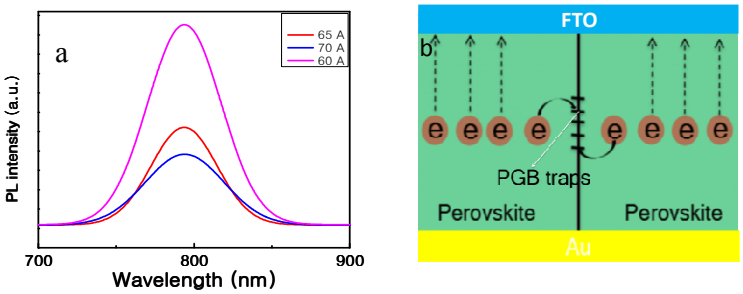

Fig. 4 (a)Steady-state photoluminescence (PL) demonstrating the amount of traps density; (b)Carrier transport mechanism diagram.

To further confirm our assumption, the steady PL measurements for $CH_3NH_3PbI_3$ films prepared with different grain size were performed. Given that perovskite films often present the characteristic of polycrystalline, [21] it is therefore universal that numerous crystal flaws exist in perovskite surface or PGB caused by dangling bonds, which have a significant influence on density of space charge in $CH_3NH_3PbI_3$ films and recombination statistics within PSCs by exchanging charge with conduction and valence bands through the emission and capture of carriers. As shown in Fig. 4a, the lower evaporation current representing larger grain size, the higher emission intensity. It is well known that the presence of emission intensity comes from the direct recombination between generated electron in conduction band and holes in valence band.

Consequently, the minor emission intensity should be affected by some nonradiative recombination related to trap centers hindering the occurrence of emission. A large grain size reduced the PGB region, and thereby decreasing the trap state density. According to the previous reports, [7,30,31] when illumination was applied, photo-generated carriers would suffer from the following physical processes in PSCs: diffusion, recombination, and being collected. As shown in Fig. 4b, the generated carriers were ideally effective collected by vertical transport in PSCs. However, a portion of electrons were injected into trap centers for recombination, and thus causing carrier lateral movement that was not in favor of carrier collection and thereby contributing to poor device performance.

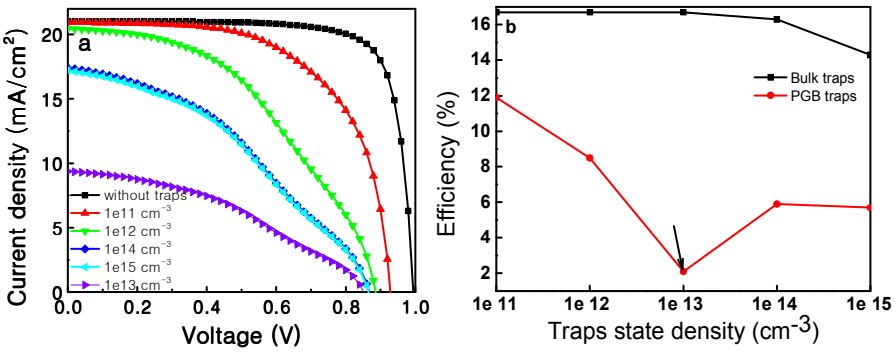

Fig. 5 (a) Simulated J-V curves of PSCs with different PGB trap state density; (b) Efficiency degeneration versus trap states density for grain bulk traps and PGB traps, respectively.

Furthermore, we simulated PSCs J-V performance based on different PGB traps state density, which were specified between $CH_3NH_3PbI_3$ grains (shown in Fig. 1a). The black edge between perovskite grains denoted the PGB region. To prepare device model simulation, we must first define a reasonable mesh corresponding to the cross section of PSCs, which covered the physical simulation domain (shown in Fig. S4). All the electrical parameters related to simulation were listed in Table S1 referring to other reported literature. [4,22,32,33] Besides, refractive index (n) and

extinction coefficient (k) spectra of $CH_3NH_3PbI_3$ films were shown in Fig. S5 according to reference 34. Fig. 5a showed the simulated J-V curves with different PGB trap state density ranging from 1e11 cm^{-3} to 1e15 cm^{-3}. It was indicated that with the increase of PGB trap state density, the device performance obviously degenerated, which had the exactly same trend with experimental result. It was therefore concluded that PGB traps indeed resulted in poor device performance. Meanwhile, we also simulated PSCs with different grain bulk trap state density range from 1e11 cm^{-3} to 1e15 cm^{-3} to compare with the situation of PGB traps. By observing the efficiency degeneration versus the trap state density, in sharp contrast, the power conversion efficiency was more pronounced sensitive to PGB traps density (shown in Fig. 5b). With regard to bulk traps, the efficiency variation was marginal as long as its value could be controlled in relative low value (<1e15 cm^{-3}), which was easily obtained by improving perovskite crystallization.

Typically, three universal recombination kinetics should be considered to accurately investigate the recombination behavior in solar cells, namely phonon transition (nonradiative generation/recombination), photon transition (radiative generation/recombination), Auger generation/recombination. [4,22] However, Auger occurs through a three particle transition, which is mainly important for wide gap semiconductor that it can be negligible in $CH_3NH_3PbI_3$. In addition, the net photon transition is a direct transition between conduction band electrons and valence band holes, which should be ascribed to equation 2, where R_{opt} represents the net photon transition rate, constant C_{opt} represents the radiative recombination factor corresponding to $CH_3NH_3PbI_3$ material no matter what value of trap density. Here, n (p) represents the concentration of electrons and holes obtained by solving coupling equation 3 to 6. Due to the identical material, we assumed that the C_{opt} was a certain value of 1.5e-10 cm^{-3} over the entire simulation. Moreover, phonon

transition occurs in the presence of trap centers within forbidden gap of perovskite, which is significantly related to our discussed PGB trap density and need to be considered carefully. In general, the net photon transition should be ascribed to equation 7 when considering the role of trap assistance, where R_{SRH} represents net phonon transition rate, C_n and C_p are specified as carrier capture cross section for electrons and holes at trap sites respectively, N_t is the density of trap states with an energy E_t in the forbidden gap (shown in Fig. S6), and $n_1(p_1)$ is the equilibrium value of electrons (holes). Consequently, the total recombination rate should be ascribed to equation 8.

$$R_{opt} = C_{opt}(np - n_{ie}^2) \quad (2)$$

$$n_{ie} = \sqrt{N_c N_v}\exp(\frac{-E_g}{2kT}) \quad (3)$$

$$E_f = \frac{E_c + E_v}{2} + \frac{kT}{2}\ln(\frac{N_v}{N_c}) \quad (4)$$

$$n = Nc\exp(\frac{E_f - E_c}{kT}) \quad (5)$$

$$n = Nv\exp(\frac{E_v - E_f}{kT}) \quad (6)$$

$$R_{srh} = \frac{CnCpNt(np - n_{ie}^2)}{Cn(n + n_1) + Cp(p + p_1)} \quad (7)$$

$$R = R_{opt} + R_{srh} \quad (8)$$

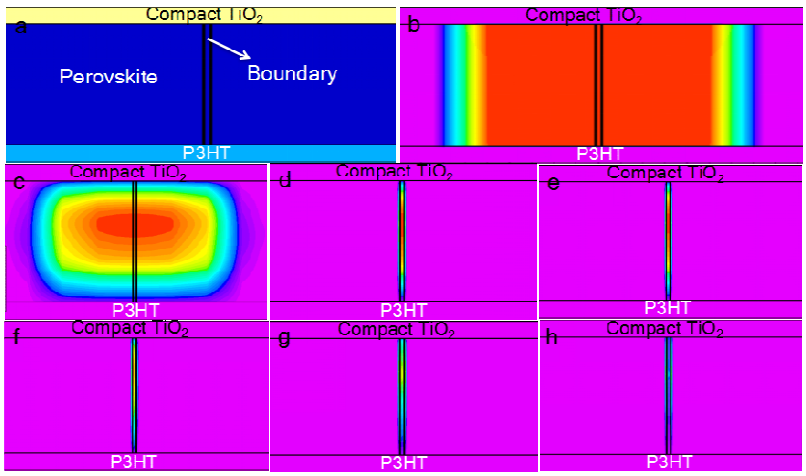

Fig. 6 Recombination rate distribution within PSCs in light illumination versus different PGB trap state density. (a) cross section diagram; (b) the carrier generation rate in illumination; (c) without traps; (d) 1e11 cm^{-3}; (e) 1e12 cm^{-3}; (f) 1e13 cm^{-3}; (g) 1e14 cm^{-3}; (h) 1e15 cm^{-3};

Fig. 6 clearly showed the total recombination rate distribution in PSCs with varying PGB trap state density ranging from 1e11 cm^{-3} to 1e15cm^{-3}. Obviously, if $CH_3NH_3PbI_3$ film possessed big enough grain size and without PGB traps in device model ideally, recombination rate distribution obeyed to gaussian distribution with the peak value at the highest generation rate (shown in Fig. 6b and c). Once PGB trap state density, however, was specified even with low value of 1e11 cm^{-3}, the recombination rate distribution had obvious variation that primary high recombination rate was concentrated on PGB region. And recombination rate inside $CH_3NH_3PbI_3$ grain bulk could be negligible when compared to PGB region, suggesting that carriers might flow from bulk to boundary region participating in high speed recombination process across the lateral direction as we mentioned in Fig. 4b. In addition, with increasing the value of PGB traps density, the recombination rate in whole PGB region became homogeneous, which were different from those in low traps density.

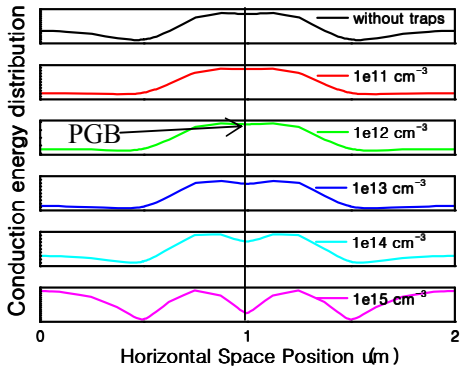

Fig. 7 Spatial conduction band energy distribution across lateral space position within PSCs.

In order to further confirm the role of PGB trap, spatial conduction band energy distribution

across lateral direction was simulated. As shown in Fig. 7, when PGB trap density was low (<1e12 cm^{-3}), there were not obvious different. In sharp contrast, with increasing the PGB trap density in $CH_3NH_3PbI_3$ photoactive layer exceeding 1e13 cm^{-3}, the conduction energy located at 1 um meaning PGB region gradually decreased. The higher trap density, the lower conduction energy. It is well recognized that electrons can spontaneously move from higher energy to lower energy. Consequently, when there were no or relative low PGB trap density, generated electrons could effectively flow and be collected. Whereas, while PGB trap density exceeded certain value (>1e13 cm^{-3}), disadvantageous electrons injection from grain bulk to PGB region happened, which leaded to carrier lateral transport and inferior carrier vertical collection, agreeing well with the above discussion.

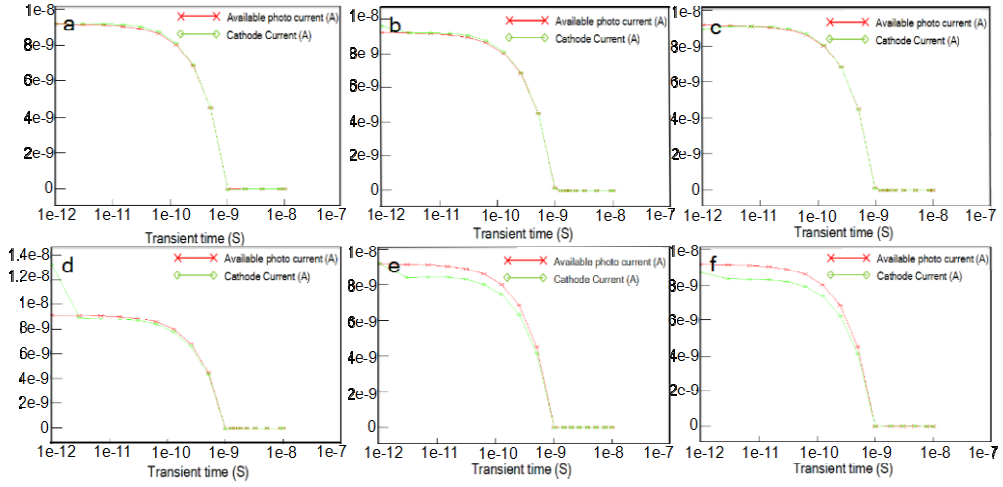

Fig. 8 Transient photo current collection efficiency versus the amount of PGB trap density. (a) without PGB traps; (b) 1e11 cm^{-3}; (c) 1e12 cm^{-3}; (d) 1e13 cm^{-3}; (e) 1e14 cm^{-3}; (f) 1e15 cm^{-3};

Moreover, transient photo current collection efficiency were probed for simulated PSCs with different PGB trap density. When 1 ns transient illumination was applied, carriers were generated, and thereby forming available photo current. As shown in Fig. 8, no matter what the value of PGB trap density, initial available photo current was invariant. Strangely, there was disordered trend

when PGB trap density was specified as 1e13 cm^{-3}, which still could not be illustrated. Anyway, to detect the simulated collected current, bias voltage was applied to cathode (FTO) to avoid the influence of current caused by forward turn-on current. As shown in Fig. 8, when PGB trap density was low (<1e12 cm^{-3}), the curves of available photo current and cathode current were almost coincidence and the weaker high cathode current was the result caused by reverse saturation current. However, the cathode current were apparent lower than available photo current when high GB trap density (>1e14 cm^{-3}) was specified, implying that inferior photo generated carrier collection efficiency that were consistent with the finding shown in Fig. 4b caused by excess carrier lateral transport. It was therefore justified to conclude that large grain size was beneficial to producing high efficiency PSCs by reducing PGB trap density and enhancing carriers vertical collection efficiency.

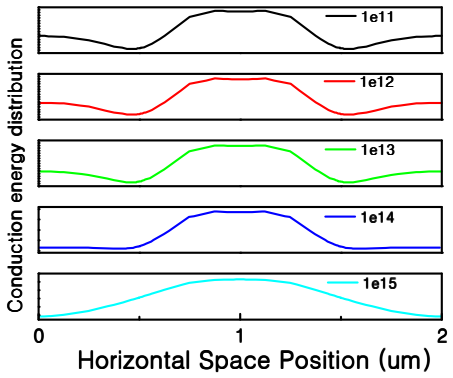

Fig. 9 Spatial conduction band energy distribution across lateral space position within PSCs possessing different bulk trap density.

I order to exclude the impact of other traps such as interface recombination, grain bulk traps on the lateral carrier transport behavior, we also analyzed the recombination rate distribution on account of grain bulk traps (shown in Fig. S7). With regard to interface recombination, all the simulation process it always was kept an invariant value of 1e6 cm^{-3}, which was a reasonable

value. Likewise, transient photo current collection efficiency versus the amount of grain bulk trap density was also included in comparison to PGB trap situation and the result was shown in Fig. S8. As shown in Fig. S7, the recombination rate distribution always exhibited gaussian distribution regardless of its trap density value. Though, the situation would vary with increasing bulk defects density. However, this situation was different from PGB trap. To more clear investigate their difference, Fig. 9 showed the spatial conduction band energy distribution across the lateral direction. It was clearly implied that there were not decreased conduction band energy within PSCs across lateral direction.

Finally, we could safely conclude that the serious PGB trap density leaded to unfavorable photo-generated carriers lateral transport, and thereby corresponding to severe carriers accumulation. Motivated by previous progress, unfavorable charge accumulation is a key factor that lead to J-V hysteresis due to the capacitive characteristic of PSCs. Thus, we considered that the high HI for PSCs possessing perovskite grain size should be also closely related with redundant PGB trap state density, which might be well demonstrated in the subsequent report.

4. CONCLUSION

In conclusion, we have demonstrated a facile and low cost method for fabricating dense $CH_3NH_3PbI_3$ films with controllable grain size ranging from 200 to 600 nm. Additionally, it is unveiled that the different $CH_3NH_3PbI_3$ grains can make a huge difference in device performance owing to possessing various different levels of PGB trap density which primarily change the electrical behavior of carriers. The large $CH_3NH_3PbI_3$ grains producing low PGB trap density are necessary for efficient PSCs. Furthermore, to investigate the original role of PGB trap, the recombination rate distribution, lateral conduction band energy distribution and transient photo current collection efficiency within $CH_3NH_3PbI_3$ films are also presented via device simulation,

which consistently reveal the fact that when PGB trap density is high, serious carrier lateral transport appear, and reducing the photo-generated carriers collection efficiency. In a word, this finding not only provides conclusive evidence for the influence of PGB traps based on physical model, but offers a predictive instruction for PSCs future development.

ASSOCIATED CONTENT

Supporting information

The XRD images of $CH_3NH_3PbI_3$ films. The absorption spectrum of $CH_3NH_3PbI_3$ films prepared by STELV with different evaporation current. The cross section SEM image of $CH_3NH_3PbI_3$ films to determine their thickness. The mesh diagram for cross section PSCs covered the physical simulation domain. The recombination rate distribution within PSCs in light illumination versus different grain bulk trap density. The transient photo current collection efficiency versus the amount of grain bulk trap density. The electrical parameter set for the simulation of PSCs. The refractive index (n) and extinction coefficient (k) spectra of $CH_3NH_3PbI_3$ film for simulation.

AUTHOR INFORMATION

Corresponding Author

*(H.C.) E-mail: caihongkun@nankai.edu.cn

Notes

The authors declare no competing financial interest.

ACKNOWLEDGEMENTS

We appreciate financial support from the National Natural Science Foundation of China (Grant No. 61504068).

REFERENCES

(1) De wolf, S.; Holovsky, J.; Moon, S. J.; Loper, P.; Niesen, B.; Ledinsky, M.; Haug, F. J.; Yum, J. H.; Ballif, C. Organometallic Halide Perovskites: Sharp Optical Absorption Edge and Its Relation to Photovoltaic Performance. J. Phys. Chem. Lett. 2014, 5, 1035-1039.

(2) Stranks, S. D.; Eperon, G. E.; Grancini, G.; Menelaou, C.; Alcocer, M. J. P.; Leijtens, T.; Herz, L. M.; Petrozza, A.; Snaith, H. J. Electron-Hole Diffusion Lengths Exceeding 1 Micrometer in

an Organometal Trihalide Perovskite Absorber. Science 2013, 342, 341-344.

(3) Beal, R. E.; Slotcavage, D. J. Leijtens, T.; Bowring, A. R.; Belisle, R. A.; Nguyen, W. H.; Burkhard, G. F.; Hoke, E. T.; McGehee, M. D. Cesium Lead Halide Perovskites with Improved Stability for Tandem Solar Cells. J. Phys. Chem. Lett. 2016, 7, 746–751.

(4) McMeekin, D. P.; Sadoughi, G.; Rehman, W.; Eperon, G. E.; Saliba, M.; Horantner, M. T.; Haghighirad, A.; Sakai, N.; Korte, L.; Rech, B.; Johnston, M. B.; Herz, L. M.; Snaith, H. J. A Mixed-Cation Lead Mixed-Halide Perovskite Absorber for Tandem Solar Cells. Science 2016, 351, 151-155.

(5) Qaid, S. M.; Al Sobaie, M. S.; Khan, M. M.; Bedja, I. M.; Alharbi, F. H.; Nazeeruddin, M. K.; Aldwayyan, A. S. Band-gap Tuning of Lead Halide Perovskite Using a Single Step Spin-Coating Deposition Process. Mater. Lett. 2016, 164, 498-501.

(6) Hsu, H. L.; Chen, C. P.; Chang, J. Y.; Yu, Y. Y.; Shen, Y. K. Two-step Thermal Annealing Improves the Morphology of Spin-coated Films for Highly Efficient Perovskite Hybrid Photovoltaics. Nanoscale 2014, 6, 10281.

(7) Du, Y.; Cai, H.; Ni, J.; Li, J.; Yu, H.; Sun, X.; Wu, Y.; Wen, H; Zhang, J. Air-Processed, Efficient $CH_3NH_3PbI_{3-x}Cl_x$ Perovskite Solar Cells with Organic Polymer PTB7 as a Hole-Transport Layer. RSC Adv. 2015, 5, 66981-66987.

(8) Chen, W.; Wu, Y.; Yue, Y.; Liu, J.; Zhang, W.; Yang, X.; Chen, H.; Bi, E.; Ashraful, I.; Gratzel, M.; Han, L. Efficient and Stable Large-Area Perovskite Solar Cells with Inorganic Charge Extraction Layers. Science 2015, 350, 944-948.

(9) Yang, W. S.; Noh, J. H.; Jeon, N. J.; Kim, Y. C.; Ryu, S.; Seo, J.; Seok, S. I. High-Performance Photovoltaic Perovskite Layers Fabricated Through Intramolecular Exchange. Science 2015,

348, 1234-1237.

(10) You, J.; Hong, Z.; Yang, M.; Chen, Q.; Cai, M. Song, T.; Chen, C.; Lu, S.; Liu, Y.; Zhou, H.; Yang, Y. Low-Temperature Solution-Processed Perovskite Solar Cells with High Efficiency and Flexibility. ACS Nano, 2014, 8, 1674–1680.

(11) Conings, B.; Drijkoningen, J.; Gauquelin, N.; Babayigit, A.; D'Haen, J.; D'Olieslaeger, L.; Ethirajan, A.; Verbeeck, J.; Manca, J.; Mosconi, E.; Angelis, F. D.; Boyen, H. Intrinsic Thermal Instability of Methylammonium Lead Trihalide Perovskite. Adv. Energy Mater. 2015, 5.

(12) Hsu, H. L.; Chang, C. C.; Chen, C. P.; Jiang, B. H.; Jeng, R. J.; Cheng, C. H. High-performance and high-durability perovskite photovoltaic devices prepared using ethylammonium iodide as an additive. J. Mater. Chem. A 2015, 3, 9271.

(13) Leguy, A. M.; Hu, Y.; Campoy-Quiles, M.; Alonso, M. I.; Weber, O. J.; Azarhoosh, P.; Schilfgaarde, M. W.; Weller, M. T.; Bein, T.; Nelson, J.; Docampo, P.; Barnes, P. R. F. Reversible Hydration of $CH_3NH_3PbI_3$ in Films, Single Crystals, and Solar Cells. Chem. Mater. 2015, 27, 3397–3407.

(14) Bryant, D.; Aristidou, N.; Pont, S.; Molina, I. S.; Chotchunangatchaval, T.; Wheeler, S.; Durrant, J. R.; Haque, S. A. Light and Oxygen Induced Degradation Limits the Operational Stability of Methylammonium Lead Triiodide Perovskite Solar Cells. Energy Environ. Sci. 2016, 10, 1039.

(15) Berhe, T. A.; Su, W. N.; Chen, C. H.; Pan, C. J.; Cheng, J. H.; Chen, H. M.; Tasi, M. C.; Chen, L. Y.; Dubale, A. A.; Hwang, B. J. Organometal Halide Perovskite Solar Cells: Degradation and Stability. Energy Environ. Sci. 2015, 9, 323-356.

(16) Ko, H. S.; Lee, J. W.; Park, N. G. 15.76% Efficiency Perovskite Solar Cells Prepared under High Relative Humidity: Importance of PbI_2 Morphology in Two-step Deposition of $CH_3NH_3PbI_3$. J. Mater. Chem. A 2015, 3, 8808-8815.

(17) Zhang, T. Y.; Yang, M. J.; Zhao, Y.; Zhu, K. Controllable Sequential Deposition of Planar $CH_3NH_3PbI_3$ Perovskite Films via Adjustable Volume Expansion. Nano Lett. 2015, 15, 3959–3963.

(18) Chen, Q.; Zhou, H.; Hong, Z.; Luo, S.; Duan, H. S.; Wang, H. H.; Liu, Y.; Li, G.; Yang, Y. Planar Heterojunction Perovskite Solar Cells via Vapor-Assisted Solution Process. J. Am. Chem. Soc. 2014, 136, 622–625.

(19) Chen, Y.; Chen, T.; Dai, L. Layer-by-Layer Growth of $CH_3NH_3PbI_{3-x}Cl_x$ for Highly Efficient Planar Heterojunction Perovskite Solar Cells. Adv. Mater. 2015, 27, 1053-1059.

(20) Ren, X.; Yang, Z.; Yang, D.; Zhang, X.; Cui, D.; Liu, Y.; Wei, Q.; Fan, H.; Liu, S. Modulating Crystal Grain Size and Optoelectronic Properties of Perovskite Films for Solar Cells by Reaction Temperature. Nanoscale, 2016, 8, 3816-3822.

(21) Shao, Y.; Fang, Y.; Li, T.; Wang, Q.; Dong, Q.; Deng, Y.; Yuan, Y.; Wei, H.; Wang, M.; Gruverman, A.; Shield, J.; Huang, J. Grain Boundary Dominated Ion Migration in Polycrystalline Organic–Inorganic Halide Perovskite Films. Energy Environ. Sci. 2016.

(22) Kim, H. D.; Ohkita, H.; Benten, H.; Ito, S. Photovoltaic Performance of Perovskite Solar Cells with Different Grain Sizes. Adv. Mater. 2015, 10, 1002.

(23) Shao, Y.; Xiao, Z.; Bi, Cheng.; Yuan, Y.; Huang, J. Origin and Elimination of Photocurrent Hysteresis by Fullerene Passivation in $CH_3NH_3PbI_3$ Planar Heterojunction Solar Cells. Nat. Commun. 2014, 5, 5784.

(24) Nie, W.; Tsai, H.; Asadpour, R.; Blancon, J.; Neukirch, A. J.; Gupta, G.; Crochet, J. J.; Chhowalla, M.; Tretiak, S.; Alam, M. A.; Wang, H.; Mohite, A. D. High-efficiency solution-processed perovskite solar cells with millimeter-scale grains. Science 2015, 347, 522-525.

(25) Liang, Z.; Zhang, S.; Xu, X.; Wang, N.; Wang, J.; Wang, X.; Bi, Z.; Xu, G.; Yuan, N.; Ding, J. A Large Grain Size Perovskite Thin Film with a Dense Structure for Planar Heterojunction Solar Cells via Spray Deposition under Ambient Conditions. RSC Adv. 2015, 5, 60562-60569.

(26) Snaith, H. J.; Abate, A.; Ball, J. M.; Eperon, G. E.; Leijtens, T.; Noel, N. K.; Stranks, S. D.; Wang, J. T.; Wojciechowski, K.; Zhang, W. Anomalous Hysteresis in Perovskite Solar Cells. J. Phys. Chem. Lett. 2014, 5, 1511-1515.

(27) Kim, H.; Park, N. Parameters Affecting I-V Hysteresis of $CH_3NH_3PbI_3$ Perovskite Solar Cells: Effects of Perovskite Crystal Size and Mesoporous TiO_2 Layer. J. Phys. Chem. Lett. 2014, 5, 2927-2934.

(28) Zhang, Y.; Liu, M.; Eperon, G. E.; Leijtens, T. C.; McMeekin, D.; Saliba, M.; Zhang, W.; Bastiani, M. D.; Petrozza, A.; Herz, L. M.; Johnston, M. B.; Lin, H.; Snaith, H. J. Charge Selective Contacts, Mobile Ions and Anomalous Hysteresis in Organic-inorganic Perovskite Solar Cells. Mater. Horiz. 2015, 2, 315.

(29) Dualeh, A.; Moehl, T.; Tetreault, N.; Teuscher, J.; Gao, P.; Nazeeruddin, M. K.; Gratzel, M. Impedance Spectroscopic Analysis of Lead Iodide Perovskite-Sensitized Solid-State Solar Cells. ACS Nano 2014, 8 , 362–373.

(30) Gonzalez-Pedro, V.; Juarez-Perez, E. J.; Arsyad, W.; Barea, E. M.; Fabregat-Santiago, F.; Mora-Sero, I.; Bisquert, J. General Working Principles of $CH_3NH_3PbX_3$ Perovskite Solar

Cells. Nano Lett. 2014, 14, 888–893.

(31) Marchioro, A.; Teuscher, J.; Friedrich, D.; Kunst, M.; Krol, R.; Moehl, T.; Gratzel, M.; Moser, J. Unravelling the Mechanism of Photoinduced Charge Transfer Processes in Lead Iodide Perovskite Solar Cells. Nat. Photonics 2014, 8, 250-255.

(32) Yang, W.; Yao, Y.; Wu, C. Q. Origin of the High Open Circuit Voltage in Planar Heterojunction Perovskite Solar Cells: Role of the Reduced Bimolecular Recombination. J. Appl. Phys. 2015, 117, 095502.

(33) Oktiawati, U. K.; Mohamed, N. M.; Burhanudin, Z. A. Effects of TiO_2 Electrode Thickness on the Performance of Dye Solar Cell by Simulation. IEEE. 2013, 406-409.

(34) Chen, C. W.; Hsiao, S. Y.; Chen, C, Y.; Kang, H. W.; Huang, Z. Y.; Lin, H. W. Optical Properties of Organometal Halide Perovskite Thin Films and General Device Structure Design Rules for Perovskite Single and Tandem Solar Cells. J. Mater. Chem. A 2015, 3, 9152-9159.